A 45° saw-dicing process applied to a glass substrate for wafer-level optical splitter fabrication for optical coherence tomography

M J Maciel[1], C G Costa[1], M F Silva[1], S B Gonçalves[1], A C Peixoto[1], A Fernando Ribeiro[1], R F Wolffenbuttel[2] and J H Correia[1]

[1] University of Minho, CMEMS-UMinho, Guimaraes, Portugal
[2] Delft University of Technology, Faculty of EEMCS, Delft, The Netherlands

E-mail: id4952@alunos.uminho.pt (M J Maciel)

CrossMark

Abstract

This paper reports on the development of a technology for the wafer-level fabrication of an optical Michelson interferometer, which is an essential component in a micro opto-electromechanical system (MOEMS) for a miniaturized optical coherence tomography (OCT) system. The MOEMS consists on a titanium dioxide/silicon dioxide dielectric beam splitter and chromium/gold micro-mirrors. These optical components are deposited on 45° tilted surfaces to allow the horizontal/vertical separation of the incident beam in the final micro-integrated system. The fabrication process consists of 45° saw dicing of a glass substrate and the subsequent deposition of dielectric multilayers and metal layers. The 45° saw dicing is fully characterized in this paper, which also includes an analysis of the roughness. The optimum process results in surfaces with a roughness of 19.76 nm (rms). The actual saw dicing process for a high-quality final surface results as a compromise between the dicing blade's grit size (#1200) and the cutting speed (0.3 mm s^{-1}). The proposed wafer-level fabrication allows rapid and low-cost processing, high compactness and the possibility of wafer-level alignment/assembly with other optical micro components for OCT integrated imaging.

Keywords: optical coherence tomography, 45° saw-dicing technology, glass roughness, MOEMS

(Some figures may appear in colour only in the online journal)

Introduction

Microelectromechanical systems (MEMS) are miniaturized integrated devices or systems that combine electrical and mechanical components. Micro opto-electromechanical systems (MOEMS) are a special class of MEMS, which adds sensing and manipulation of optical signals in a very small device [1, 2]. Examples of MOEMS applications include: micro-mirrors [3], micro beam-splitters (MBS) in micro interferometers [4, 5], optical scanners [6], scanning micro-mirrors [7, 8] and micro spectrometers [9]. The merits of MOEMS fabrication, as compared to conventionally fabricated bulky opto-electromechanical systems, are: miniaturized dimensions, reduced weight and high speed of operation. Moreover, the use of photolithography on wafers enables batch production of large numbers of identical devices, which results in low unit cost. Finally, a CMOS compatible MOEMS process would enable on-chip integration of optical component and readout, thus resulting in highly compact systems that are robust and have integrated intelligence [2, 5]. The technology

presented in this paper is based on the use of a glass substrate, hence, is not aiming on a single-wafer CMOS-compatible MOEMS.

The early application areas of MOEMS were in optical communication and micro-mirror arrays [10]. The current directions are mainly on the use in miniaturized instruments and devices for biology, medicine, chemistry and physics [5]. This trend towards the miniaturization of optical subsystems has significantly affected the design of medical tools, but has also become a key issue on biomedical imaging. Miniaturization of medical devices has made minimally invasive and non-invasive techniques possible. The merits of such approaches for examining a patient are: the reduced side effects, by inserting a much smaller tool or no tool at all, and the portability, which is limited considering the bulky devices. A modern medical imaging technique to which this technological development has been particularly beneficial is optical coherence tomography (OCT) [11]. MOEMS has started to play an important role in the development of OCT miniaturized systems. At the core of these applications is light interferometry, which is a key optical phenomenon for which the miniaturized scanning interferometers are the controlling manipulating devices [3, 5, 6, 12].

OCT is an optical imaging modality that enables the reconstruction of the cross-sectional view of biological tissue, by measuring the echo time delay and magnitude of back-reflected light. OCT is comparable to ultrasound imaging, but makes use of near infrared (NIR) light instead of acoustic waves [11, 13–15]. The OCT concept was firstly presented by Hung *et al*, in 1991 [16] and the first *in vivo* image was presented by Fercher *et al* in 1993 [17]. As the propagation velocity of light is much higher than that of sound, the direct measurement of the echoes cannot be performed electronically, as in ultrasound imaging. Therefore, the operation principle of OCT is based on the interference between two signals: one from the object under investigation and another from a local reference. This concept is referred as low-coherence interferometry (LCI) [11, 13]. In LCI, the light back-reflected from inside a specific object under investigation is measured by correlating it with light that has travelled a reference path of well-known length. The conventionally used configuration of LCI for OCT applications employs the Michelson interferometer for interfering the two light beams. A NIR source emits a light wave to a beam-splitter (BS), which divides the light into two waves. One part travels to a reference mirror, which reflects the light wave directly back to the BS. The second wave travels to the sample being analysed. Depending on the optical properties of the sample, light can be absorbed, refracted and reflected. The back-reflected light from the sample interferes with the reflected light from the reference mirror, and the interference is finally detected with a detector system at the output of the Michelson interferometer.

There are two approaches for implementing LCI in OCT: time domain (TD-OCT) and frequency domain (FD-OCT), as represented in figure 1. The FD-OCT approach can be implemented in two system configurations: based on a spectrometer (SD-OCT), or based on a swept source or tunable laser (SS-OCT). Although the initial OCT generations were operated

in TD, present systems are operated in the FD, because the need of a moving mirror, which is an essential component in TD-OCT for depth scanning, is avoided [11, 13, 14, 18].

State-of-the-art systems are bulky and are operated as FD-OCT, using either a spectrometer or a tunable laser [19]. These systems are mainly used in clinical practice, particularly in ophthalmology [20]. This paper is intended to contribute to the current trend of scientific research towards OCT miniaturization using MOEMS technologies [6, 21], which would make the concept suitable for application in other medical fields, such as endoscopy [22] and dermatology [19].

The 45° saw dicing process is introduced in this paper and optimized for the fabrication of the optical components that are required in a micro Michelson interferometer for use in a complete FD-OCT system. The wafer-level fabrication is based on two simple MEMS technologies: the saw dicing of a glass substrate, using custom made dicing blades, and thin film deposition of a dielectric multilayer and metallic layers. A similar 45° saw dicing process of glass wafer was already presented in literature [23–25]. To the best of our knowledge, this is the first attempt for using such a technology for OCT applications.

Methods

Design and architecture

The micro Michelson interferometer is obtained with a micro BS and micro mirrors, as presented in figure 2. This MOEMS prototype is intended for the NIR range of 800–900 nm, which is typically used in FD-OCT applications. The use of 45° surfaces is selected for enabling lateral propagation of the reflected light beams, which enables vertical and horizontal separation of the incident beam and would simplify future integration with other micro optical components [24–27]. The wafer level dicing of glass substrate is carried out by custom-made 45° dicing blades. As is demonstrated in figure 1, a dielectric multilayer is deposited onto the central 45° surface, which allows the splitting of the incident beam. Additionally, metal layers are deposited onto two other 45° surfaces for operation as micro-mirrors for sensing purposes and for directing the light beam to the output of the Michelson interferometer. Another micro-mirror is deposited at the bottom of micro BS for defining the reference path by reflecting the beam directly from the optical source.

Different dielectric multilayers can be deposited onto the central 45° surface, depending on the split ratio required for a specific FD-OCT application (polarizing or non-polarizing dependent). For the proposed prototype, the split ratio should be wavelength-independent over the specified spectrum (800–900 nm). Moreover, the multilayer should be tolerant to fluctuations in the (optical) layer thicknesses, which implies a minimum number of layers to be used. A combination of low and high refractive indexes materials was used for obtaining a 50/50 non-polarizing split ratio. Silicon dioxide (SiO_2) and titanium dioxide (TiO_2) were the materials chosen for the implementation of the low and high refractive indexes, respectively. A continuous target was defined to obtain a
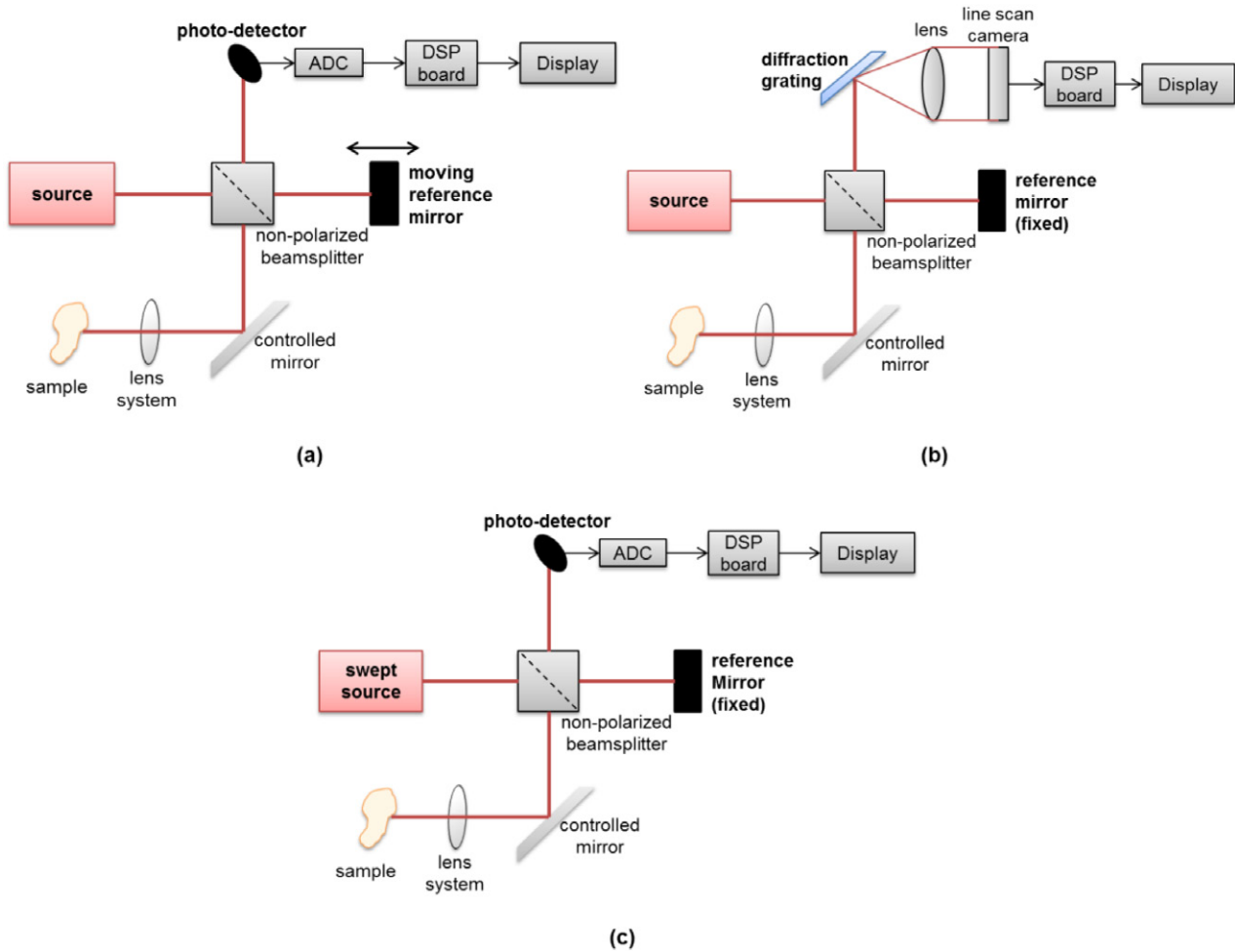
Figure 1. Block diagrams of the different OCT configurations: (a) the TD-OCT; (b) FD-OCT in SD-OCT; (c) FD-OCT in SS-OCT. The ADC is an analog-to-digital converter and the DSP is a digital signal processor.
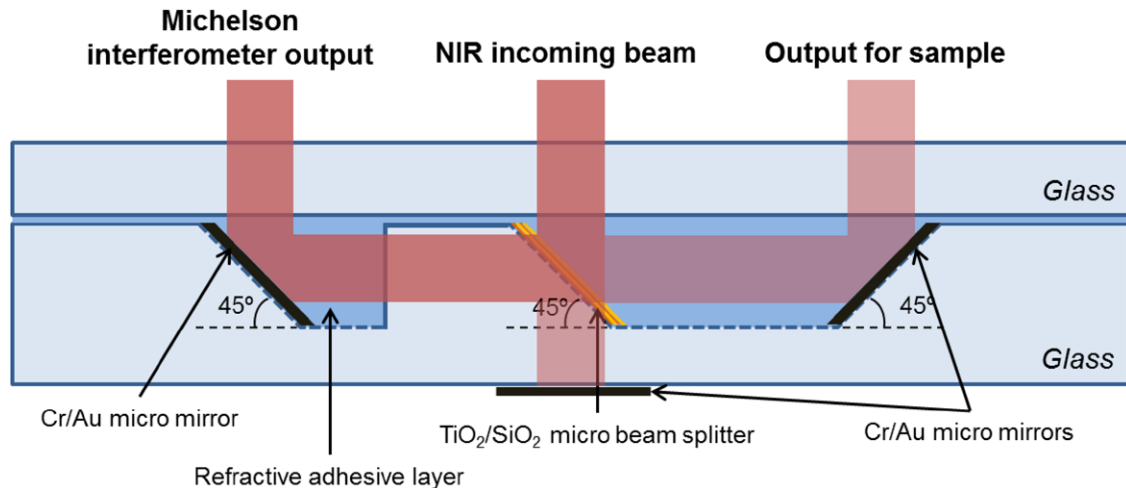

Figure 2. Design and architecture of the proposed micro Michelson interferometer on a glass substrate. A refractive adhesive layer is used to avoid the deflection of the beam.

50% transmittance/ reflectance in the S and P polarizations, while an incidence angle of 45° was defined in the setting of TFCalc™ simulation tool. After optimization, a split ratio of approximately 50/50 was obtained in the specified NIR region with only four thin-film layers, with values of the layer thickness as listed in table 1. An average reflectance of 49.6% was

obtained with this multilayer over the NIR range. The NIR micro-mirror was obtained with an initial adhesion thin layer of chromium (Cr) and a layer of gold (Au). The TFCalc™ simulations reveal that a stack of 50 nm/250 nm thickness of Cr/Au has a reflectance higher than 97% over the specified spectral range.
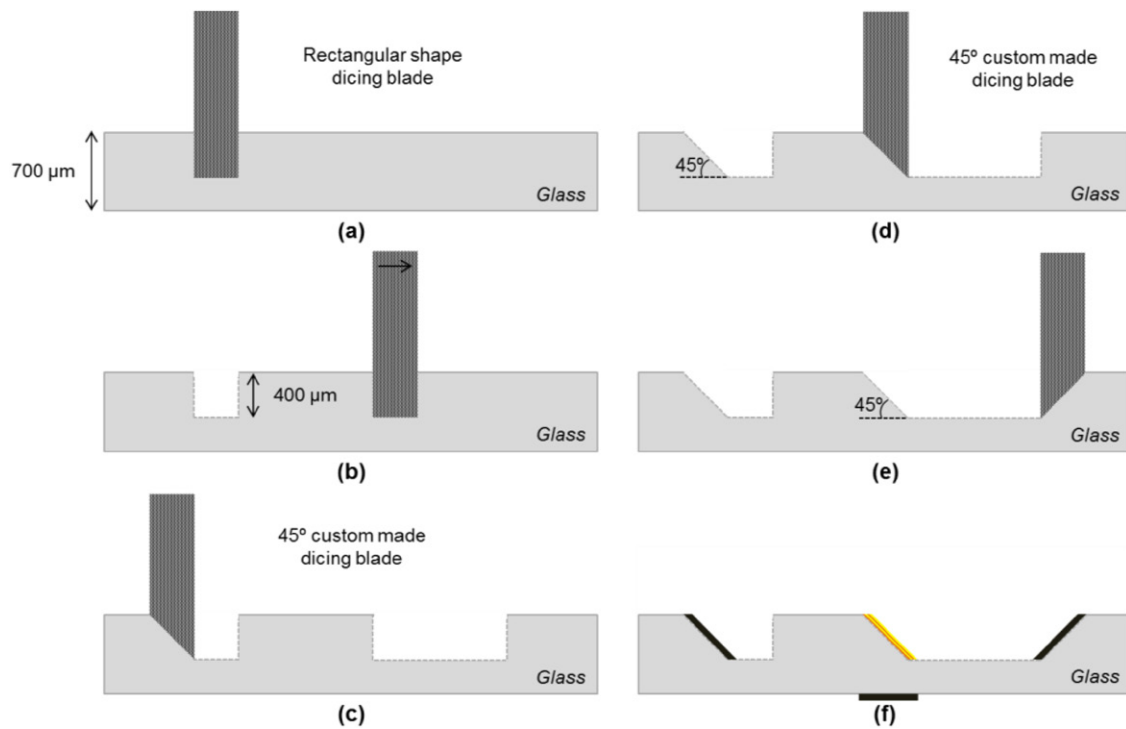
Figure 3. MOEMS fabrication method: (a)–(e) the saw dicing process with 45° custom made and conventional rectangular shape dicing blades; (f) thin film deposition of the dielectric multilayer (TiO$_2$/SiO$_2$) and metallic layers (Cr/Au).

Table 1. TiO$_2$/SiO$_2$ multilayer[3] optimized for 50/50 split ratio in NIR range (800–900 nm). The required split ratio was obtained with only four layers. The simulation was performed in TFCalc™.

Layer	1	2	3	4
Material	TiO$_2$	SiO$_2$	TiO$_2$	SiO$_2$
Thickness (nm)	82	181	83	165

Table 2. Technical details of three different dicing blades.

Dicing blade	Grit size	Thickness (μm)	Basic shape[a]	Angle shape (°)
B1V863S3 SD800	#800	500		45
B1V863S3 SD1200	#1200	500		45
B1A863S3 SD800	#800	500		0

[a] Cross-sectional view.

MOEMS fabrication

The fabrication of the proposed micro Michelson interferometer on a glass substrate (borosilicate glass; thickness = 700 μm; diameter = 4 inch; 2-side polished) is based on two simple microfabrication technologies: the saw dicing of glass substrate and thin film deposition. The complete MOEMS fabrication flow is presented in figure 3. The glass wafer was firstly micromachined using an automatic Disco DAD 2H/6T dicing saw and 45° custom made dicing blades. Selecting a compromise between the dicing speed and the grit size of the blade is essential for process optimization in terms of final surface quality. For this purpose, tests have been performed using 45° custom made and conventional rectangular shape blades. The second part of micro fabrication consists on the deposition of the dielectric multilayer and metallic layers, for obtaining the micro-BS and micro-mirrors, respectively. The dielectric multilayer of TiO$_2$/SiO$_2$ was deposited by RF magnetron sputtering at 13.56 MHz. A Ti-metal target of high purity (99.7%) was used for TiO$_2$ reactive magnetron sputtering, using a gas flow of 10 and 20 sccm for sputtering

(Ar—argon) and reactive (O$_2$—oxygen) gases, respectively. For SiO$_2$ magnetron sputtering, a target of SiO$_2$ (99.9995% of purity) and a gas (Ar) flow rate of 15 sccm were used. The electron beam technique was used for Cr deposition, with Cr pellets placed inside a crucible based in graphite. Finally, the Au layer was deposited by thermal evaporation, using a gold pellet placed in the boat heater.

45° saw dicing

The saw dicing process of glass substrate was optimized for a minimum roughness, to result in low scattering at the optical surface after the deposition of the dielectric and metallic layers. Three different custom made blades with two different grit sizes were used (obtained from Disco technologies, Japan) to perform the 45° and 0° final surfaces. The grit size basically defines the roughness distribution over the blade. The blade reference number and some technical details of the different blades are listed in table 2. The thickness of 45° shaped blades was chosen according to the height required in the final microstructure.

[3] The refractive indexes of SiO$_2$ and TiO$_2$ used in the simulation were measured by *Lemarchand* (http://refractiveindex.info/?shelf=main&book=SiO2&page=Lemarchand) and *Devore* (http://refractiveindex.info/?shelf=main&book=TiO2&page=Devore-o).
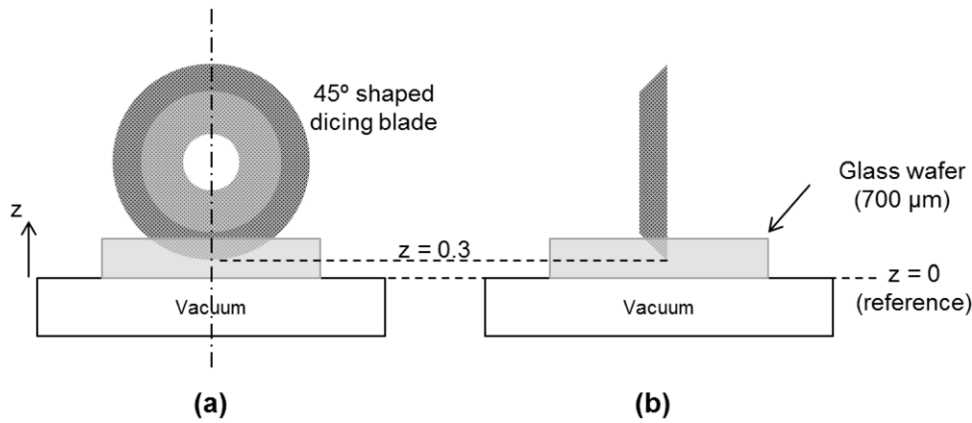
Figure 4. Schematic of the dicing cuts performed with Disco DAD 2H/6T dicing saw: (a) front and (b) cross-sectional view.

Table 3. Roughness measurements (nm) of the dicing cuts performed with the dicing blade B1A8 SD800 at different cutting speeds (mm s^{-1}).

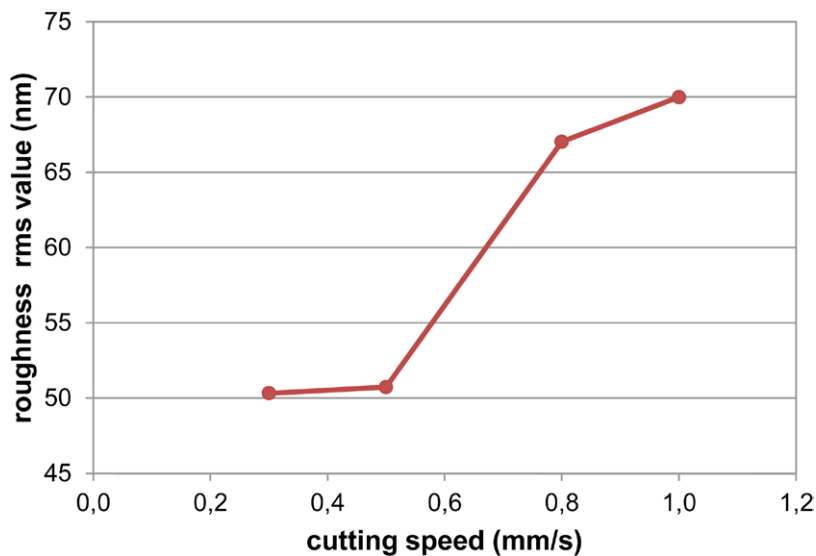| Cutting speed (mm s^{-1})	Roughness measurements (nm)						rms (nm)
0.30	51.73	41.31	52.69	49.85	54.76	50.48	50.32
0.50	49.25	49.31	48.02	53.41	51.89	52.26	50.73
0.80	63.17	70.51	63.48	69.38	68.66	66.62	67.03
1.00	65.39	68.32	69.21	73.76	66.30	76.33	70.00

Figure 5. Roughness variation according to the cutting speed for the rectangular shape blade with the reference B1A8 SD800.

The diamond grit size and the cutting speed are the two parameters that have a great influence on the roughness of the final surface. Different cutting speeds were tested for each dicing blade in order to study the influence of grit size and cutting speed on the surface's quality. The cuts were carried out using an automatic Disco DAD 2H/6T dicing saw, which permits high precision cuts for miniaturized applications. For each pair grit size/ cutting speed, six roughness measurements were performed with a profilometer (Dektak model 150 with a 12.5 μm radio stylus, using a force of 3 mg). The measurements were made at six randomly selected places of two cuts. After that, the mean was calculated for each pair cutting speed/dicing blade. Figure 4 schematically shows the fabrication process with the appropriate setting of the variable

z-index. For a cutting height of 400 μm, a z-index of 300 μm should be defined in the dicing program, since the thickness of the glass wafer is 700 μm. For the rectangular shape blade (B1A863S3 SD800) four different cutting speeds were tested in the range from 0.3 to 1.0 mm s^{-1}. For the 45° shaped blades (B1V863S3 SD800/1200) three speeds were tested (0.3, 0.5 and 0.8 mm s^{-1}).

Results and discussion

The roughness measurements of the dicing cuts performed with the rectangular shape blade B1A8 SD800 are listed in table 3. Figure 5 shows the roughness behaviour at varying cutting speed.

Table 4. Roughness measurements (nm) of the dicing cuts performed with the 45° shaped dicing blade B1V8 SD800 at different cutting speeds (mm s^{-1}).

Cutting speed (mm s^{-1})	Roughness measurements (nm)						rms (nm)
0.30	24.99	23.30	26.32	27.98	22.37	25.90	25.21
0.50	28.96	23.22	26.49	30.37	31.07	28.62	28.24
0.80	42.27	32.62	42.10	41.40	35.36	42.51	39.57

Table 5. Roughness measurements (nm) of the dicing cuts performed with the 45° shaped dicing blade B1V8 SD1200 at different cutting speeds (mm s^{-1}).

Cutting speed (mm s^{-1})	Roughness measurements (nm)						rms (nm)
0.30	19.39	20.77	21.77	17.64	17.93	20.72	19.76
0.50	24.69	27.15	23.5	27.82	27.62	29.12	26.72
0.80	30.03	33.49	28.93	31.45	32.56	29.77	31.08
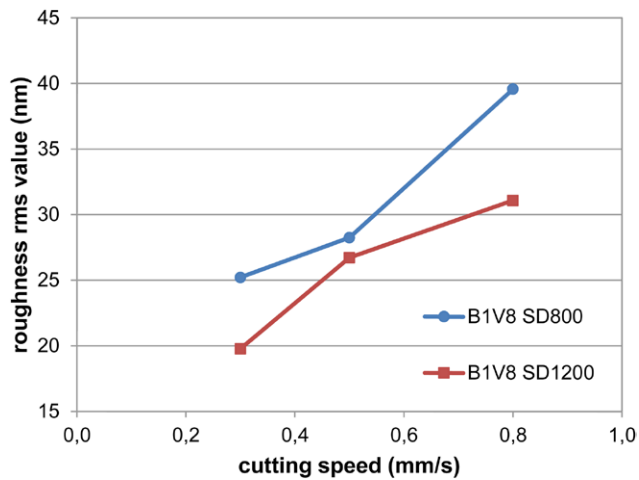
Figure 6. Roughness variation according to grit size and cutting speed for the 45° custom made dicing blades B1V8 SD800 and B1V8 SD1200.

The blades with references B1V8 SD800/1200 were tested with the same fabrication parameters (height and cutting speed), in order to obtain a comparative analysis between grit size and cutting speed. Tables 4 and 5 contain the roughness measurements of the blades B1V8 SD800 and B1V8 SD1200, respectively. The average (rms value) of the six measurements was calculated and used to obtain the curves in figure 6, where the variation as a function of cutting speed is compared between the two 45° custom made blades.

Generally, it can be concluded that the roughness is directly proportional to the cutting speed of the saw dicing process (i.e. the lowest roughness values are obtained with the lowest cutting speed). The results indicate a high roughness of the surfaces performed with the conventional rectangular shape blade B1A8 SD800. The highest roughness obtained was 76.33 nm with a cutting speed of 1.0 mm s^{-1}, while the lowest roughness obtained was 41.31 nm with the lowest cutting speed of 0.3 mm s^{-1}. The effect of cutting speed become significant for cutting speeds in the range from 0.5 to 0.8 mm s^{-1}, as is shown in figure 5. This type of rectangular shape blade is used to obtain the horizontal surfaces, which separate the different micro optical components of the MOEMS proposed in this paper.

When the results of the rectangular shape blade are compared to the 45°-shaped blade with the same grit size (#800), it can be noted that the roughness is lower in the cuts performed with B1V8 SD800 than in the cuts performed with the blade B1A8 SD800. Comparing the two 45° shaped blades, with different grit size (#800 and #1200) reveals that the two 45° dicing blades have very similar velocity-roughness characteristics, as the rectangular shape blade. The results of blade B1V8 SD800 show a lowest roughness of 22.37 nm with a cutting speed of 0.3 mm s^{-1} and a highest roughness of 42.51 nm at 0.8 mm s^{-1}. The dicing blade B1V8 SD1200 allowed a lowest roughness of 17.64 nm at 0.3 mm s^{-1} and a highest value of 33.49 nm at 0.8 mm s^{-1}. Comparing the same cutting speed in these two blades, the thinnest grit size (#1200) revealed a lower roughness (nm) for all three cutting speeds considered. Therefore, the roughness reduces with thinner the grit size (i.e. higher grit number), as is shown in figure 6. The selected operating mode, based on lowest roughness, was with the thinnest grit size (B1V8 SD1200) and with the lowest cutting speed (0.3 mm s^{-1}).

Figure 6 shows the minimum average roughness with an rms-value of 19.76 nm. Microscope photographs on some of the cuts used in the roughness optimization process (obtained with a Leica M80™ stereo microscope and processed in Leica LAS™ software) are shown in figure 7. A difference in *z*-index should be selected for cuts performed with rectangular shape blades and those with 45°-shaped blades. The appropriate value is 0.2 mm. Basically, the *z*-index should be re-adjusted in the final cuts, according to the height required for the final microstructure.

After the roughness analysis and the re-adjustment of the dicing cuts parameters, the complete MOEMS was fabricated and the result is presented in figure 8. The height of the 45° cuts is 400 μm and the distance between the different tilted surfaces is approximately 2 mm. An average angle (rms value) of 45.07 ± 0.20° was obtained in the final, tilted surfaces. A combination of high grit size and low cutting speed and the thickness of the blades allows a high precision of the 45° saw dicing process. In fact, the roughness of the final surface is also correlated with the precision of the process, as can be concluded from the results.
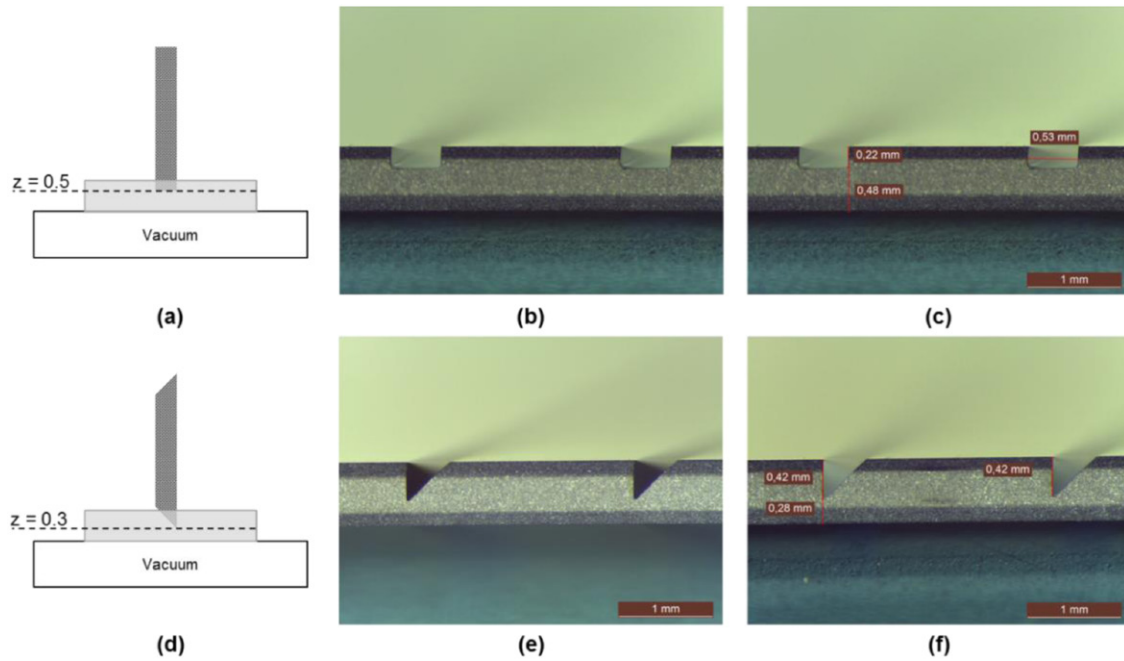
Figure 7. Optimization process of the saw dicing process: (a) set-up of the cuts performed with the rectangular shape blade; (b) and (c) microscope photographs of two rectangular cuts used for roughness measurements; (d) set-up of 45° saw dicing cuts; (e) and (f) microscope photographs of two 45° dicing cuts, used for roughness analysis.
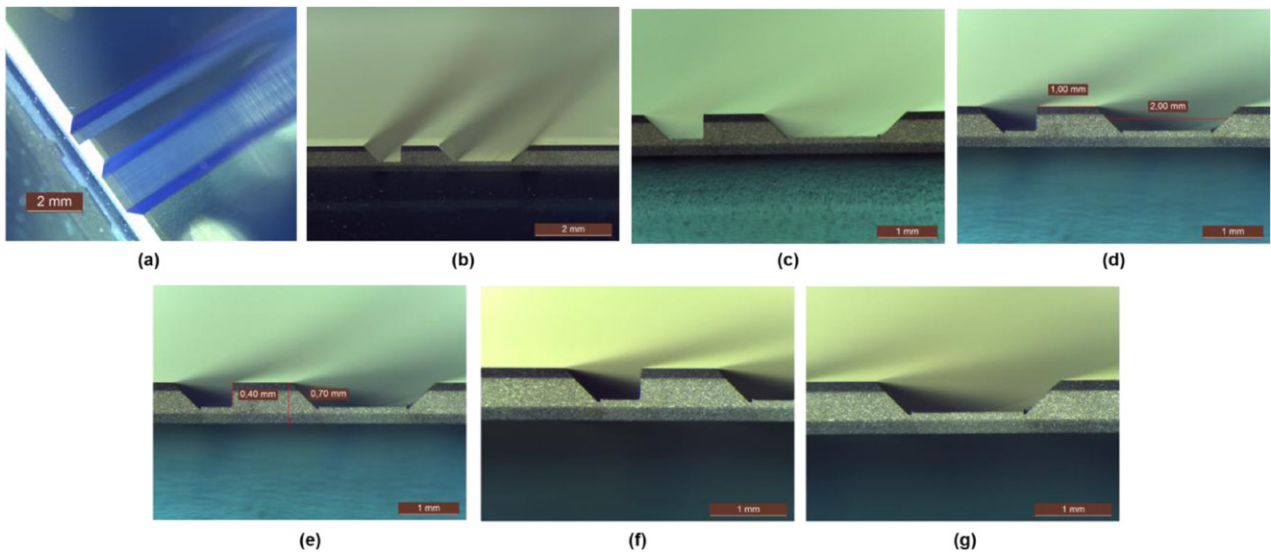

Figure 8. Microscope photographs of the final MOEMS: (a) and (b) top views; (c) cross-section view; (d) distance between different cuts; (e) height measurement of the grooves; (f) and (g) magnified Leica photographs.

Conclusion

In this paper a roughness analysis was performed on dicing cuts that result from micro fabrication based on the 45° saw dicing of glass substrate using custom-made dicing blades. The intended application of the MOEMS presented in this work is OCT miniaturization and integration on a single micro-chip. The results demonstrate that the combination of dicing blade's grit size and the cutting speed of the dicing process have a major influence in the quality of the final cut surfaces. A minimum roughness of 19.76 nm rms was obtained with the finest grit size available (#1200) and the lowest setting of the cutting speed (0.3 mm s^{-1}). The saw dicing process was fully characterized to enable the reduction of the structural distortions in the entire process, particularly in the consequent thin film deposition. With the roughness analysis and optimization, a reduced structural distortion can be assured. The roughness in the final surface reduces with the structural distortion.

The 45° saw dicing process of a glass substrate proved to be a highly suitable MEMS process for future micro integration of different optical components in a single microsystem.

Moreover, it was shown that the Michelson interferometer can be obtained with a micro BS formed by a four layer design with TiO_2/SiO_2 combined with Cr/Au micro mirrors for appropriately directing the light beams through the structure. The micro BS presented in this paper was designed for 50/50 non-polarizing split ratio. Depending on the requirements of the application, different split ratios can be easily obtained by changing the dielectric multilayer design. The use of the 45° surfaces allows the horizontal/vertical separation of the incident beam, which is a crucial factor for future integration with other optical components in a complete FD-OCT microsystem.

The fabricated MOEMS offers high compactness and the possibility of wafer-level alignment/assembly, which makes it highly suitable for vertically integrated imaging micro-instruments. To the best of our knowledge this is the first steps towards OCT miniaturization using optical MEMS technologies on a glass substrate. The future work and motivation is the integration of the proposed micro Michelson interferometer with a micro spectrometer, using MEMS technologies, in a complete SD-OCT micro-system.

Acknowledgments

References

[1] Song I-H, Peter Y-A and Meunier M 2007 Smoothing dry-etched microstructure sidewalls using focused ion beam milling for optical applications *J. Micromech. Microeng.* **17** 1593–7

[2] Schuler L P, Milne J S, Dell J M and Faraone L 2009 MEMS-based microspectrometer technologies for NIR and MIR wavelengths *J. Phys. D: Appl. Phys.* **42** 133001

[3] Mu X, Sun W, Feng H, Yu A, Chen K W S, Fu C Y and Olivo M 2011 MEMS micromirror integrated endoscopic probe for optical coherence tomography bio-imaging *Sensors Actuators* A **168** 202–12

[4] Lullin J, Bargiel S, Lemoal P, Perrin S, Albero J, Passilly N, Froehly L, Lardet-Vieudrin F and Gorecki C 2015 An electrostatic vertical microscanner for phase modulating array-type Mirau microinterferometry *J. Micromech. Microeng.* **25** 115013

[5] Sabry Y M, Khalil D and Bourouina T 2015 Monolithic silicon-micromachined free-space optical interferometers onchip *Laser Photon. Rev.* **9** 1–24

[6] Xu Y, Singh J, Premachandran C S, Khairyanto A, Chen K W S, Chen N, Sheppard C J R and Olivo M 2008 Design and development of a 3D scanning MEMS OCT probe using a novel SiOB package assembly *J. Micromech. Microeng.* **18** 125005

[7] Zhang C, You Z, Huang H and Li G 2010 Study on a two-dimensional scanning micro-mirror and its application in a MOEMS target detector *Sensors* **10** 6848–60

[8] Chi Z, Gaofei Z and Zheng Y 2009 A two-dimensional micro scanner integrated with a piezoelectric actuator and piezoresistors *Sensors* **9** 631–44

[9] Wolffenbuttel R F 2005 MEMS-based optical mini- and microspectrometers for the visible and infrared spectral range *J. Micromech. Microeng.* **15** S145–52

[10] Ollier E 2002 Optical MEMS devices based on moving waveguides *IEEE J. Sel. Top. Quantum Electron.* **8** 155–62

[11] Wojtkowski M 2010 High-speed optical coherence tomography: basics and applications *Appl. Opt.* **49** D30–61

[12] Liu L, Wu L, Sun J, Lin E and Xie H 2011 Miniature endoscopic optical coherence tomography probe employing a two-axis microelectromechanical scanning mirror with through-silicon vias *J. Biomed. Opt.* **16** 026006

[13] Gambichler T, Jaedicke V and Terras S 2011 Optical coherence tomography in dermatology: technical and clinical aspects *Arch. Dermatol. Res.* **303** 457–73

[14] Hamdan R, Gonzalez R G, Ghostine S and Caussin C 2012 Optical coherence tomography: from physical principles to clinical applications *Arch. Cardiovasc. Dis.* **105** 529–34

[15] Podoleanu A G 2012 Optical coherence tomography *J. Microsc.* **247** 209–19

[16] Huang D *et al* 1991 Optical coherence tomography *Science* **254** 1178–81

[17] Fercher A, Hitzenberger C, Drexler W, Kamp G and Sattmann H 1993 *In vivo* optical coherence tomography *Am. J. Ophthalmol.* **116** 113–4

[18] Tomlins P H and Wang R K 2005 Theory, developments and applications of optical coherence tomography *J. Phys. D: Appl. Phys.* **38** 2519–35

[19] Akca B I *et al* 2012 Toward spectral-domain optical coherence tomography on a chip *IEEE J. Sel. Top. Quantum Electron.* **18** 1223–33

[20] Gabriele M L, Wollstein G, Ishikawa H, Xu J, Kim J, Kagemann L, Folio L S and Schuman J S 2010 Three dimensional optical coherence tomography imaging: advantages and advances *Prog. Retin. Eye Res.* **29** 556–79

[21] Yurtsever G, Dumon P, Bogaerts W and Baets R 2010 Integrated photonic circuit in silicon on insulator for Fourier domain optical coherence tomography *Proc. SPIE* **7554** 75541B-1–5

[22] Gilchrist K H, McNabb R P, Izatt J A and Grego S 2009 Piezoelectric scanning mirrors for endoscopic optical coherence tomography *J. Micromech. Microeng.* **19** 1–11

[23] Baranski M, Bargiel S, Passilly N, Guichardaz B, Herth E, Gorecki C, Jia C, Frömel J and Wiemer M 2014 Wafer-level fabrication of microcube-typed beam-splitters by saw-dicing of glass substrate *IEEE Photonics Technol. Lett.* **26** 100–3

[24] Bargiel S, Baranski M, Passilly N, Gorecki C, Wiemer M, Frömel J, Wünsch D and Wang W 2015 Technological platform for vertical multi-wafer integration of miniature imaging instruments *SPIE Photonics West MOEMS and Miniaturized Systems* **9375** 93750L-1–8

[25] Glebov A L, Roman J, Lee M G and Yokouchi K 2005 Optical interconnect modules with fully integrated reflector mirrors *IEEE Photonics Technol. Lett.* **17** 1540–2

[26] Chuang Y-J, Huang S-H, Chen Y-C and Hung K-Y 2012 Application of the inclined exposure and molding process to fabricate a micro beam-splitter with nanometer roughness *Microsyst. Technol.* **19** 461–70

[27] Wang F, Liu F and Adibi A 2009 45 degree polymer micromirror integration for board-level three-dimensional optical interconnects *Opt. Express* **17** 10514–21